Quadrupolar NMR relaxation of aqueous ¹²⁷I⁻, ¹³¹Xe, and ¹³³Cs⁺: A first-principles approach from dynamics to properties

Adam Philips^a, and Jochen Autschbach*^a

Department of Chemistry
 University at Buffalo

 State University of New York
 Buffalo, NY 14260-3000, USA
 email: jochena@buffalo.edu

Abstract: Quadrupolar NMR relaxation rates were computed for aqueous ¹³³Cs⁺, ¹³¹Xe, and ¹²⁷I⁻ via Kohn-Sham (KS) density functional theory-based ab-initio molecular dynamics (aiMD) and KS calculations of the electric field gradient (EFG) tensors along the trajectories. The resulting rates are within a factor of one to three of the experimental values and can be compared to available results from classical dynamics and EFGs from electrostatic models with corrections via Sternheimer antishielding factors. Relativistic effects are shown to have an enhancing effect on the magnitude of the EFGs. An analysis of the EFGs was carried out in terms of localized molecular orbitals, to elucidate contributions from the solvent versus solute polarization and assess the validity of the Sternheimer approximation for these systems.

1 Introduction

NMR relaxation has been studied extensively for decades both experimentally and theoretically. NMR relaxation rates (or times) and the associated line widths in solution spectra are useful probes of the dynamic structure around the resonant nuclei in liquids and solids. A majority of elements in the periodic table have nuclei with spin $S \ge 1$, which is accompanied by an electric nuclear quadrupole. The nuclear quadrupole interacts with an electric field gradient (EFG), if present. The latter is caused by a deviation of the electric charge distribution surrounding the nucleus from high symmetries such as spherical, octahedral, or tetrahedral. While other interactions, e.g. nuclear magnetic dipole-dipole coupling, chemical shift anisotropy (CSA), spinrotation (SR), can affect nuclei of all types, the quadrupolar mechanism is known to dominate the relaxation when present. (We disregard nucleus-electron magnetic interactions in paramagnetic systems, which can be very strong.)

In solution, quadrupolar relaxation is driven by fluctuations of the EFG around a quadrupolar nucleus caused by the microscopic dynamics of surrounding solvent molecules or ions carrying partial or full electric charges, and the corresponding distortion of the election density around the quadrupolar nucleus. For many decades, the prevailing theoretical approaches to computing and interpreting the quadrupole-EFG coupling—and therefore the relaxation rates in solutions—were

electrostatic models. These models inherently neglect the microscopic details of the dynamics which drive relaxation. Many studies^{1–18} have utilized molecular dynamics (MD) simulations in an effort to explicitly treat solute-solvent interactions on the time scale of the EFG fluctuations. Most of these relied on force-field based methods parameterized for a limited number of—primarily—main group elements. With the increasing power and availability of computational resources, ab-initio MD (aiMD) methods have become increasingly feasible for simulating spectroscopic phenomena in liquids which depend on subtle dynamic interactions on the femtoto nanosecond time scale. Local EFG fluctuations in liquids are among these kind of phenomena.

Computations of EFGs via electrostatic models have been widespread. For solvated atoms and ions, these methods employ empirical approximations such as Sternheimer anti-shielding factors γ , 19, 20 rooted in perturbation theory, to account for internal electronic polarization of the analyte induced by the surrounding charges. This approach has met with some success for 'hard'—i.e., comparatively weakly polarizable—metal ions such as Li⁺, K⁺, Mg²⁺ or transition metal ions. Rotenberg et al.¹³ validated the approximation for such systems insofar as to show that a linear relationship exists between the external EFG as calculated via a polarizable ion model and the true total EFG obtained via all-electron DFT calculations. However, the Sternheimer model has usually only been applied in a (usually lowest-order) long-range approximation, with the corresponding Sternheimer factors labeled as γ_{∞} . The model generally assumes that the EFG is caused through polarization of a previously spherical electron charge density by an external charge at a given distance. In the long-range Sternheimer approximation, the external EFG is then simply scaled by $(1 + \gamma_{\infty})$ to account for the polarization effects. Note that γ_{∞} is far from being a small correction. For instance, values of -5.45, -4.12, and -18.79 were given in Reference 21 for Na⁺, Mg²⁺, and Ca²⁺, respectively, including corrections for crystal embedding. The Sternheimer model neither accounts for solute polarization due to steric effects, nor for EFGs due to partially covalent solvent-solute interactions such as hydrogen bonds. The EFG, being a molecular property that is very sensitive to structure and bonding, generally requires a fully quantum theoretical approach to treat the electronic effects for all but the least polarizable solutes. Furthermore, for heavier elements such as ¹²⁷I⁻, ¹³¹Xe, and ¹³³Cs⁺, studied in this work, relativistic effects may play an important role. 22-24

For the reasons outlined in the previous paragraph, this work follows a fully first-principles approach developed and utilized in our previous work in which we computed quadrupolar NMR relaxation rates for aqueous ²³Na⁺ and ³⁵Cl⁻, ¹⁴N in azole-type molecules, as well as for ²H and ¹⁷O in heavy water which also relax via the quadrupolar mechanism. ^{15–18} In this approach, the systems are simulated via Kohn-Sham (KS) density functional theory (DFT) based MD, and EFG calculations on the MD configurations ('snapshots') are also performed at the KS-DFT level, in order to get access to the EFG time autocorrelation functions (ACFs) that ultimately determine

the relaxation rates. For the present study, these snapshots are extracted from the MD as finite solute-solvent clusters and treated at the hybrid DFT level with an all-electron scalar relativistic Hamiltonian. Even in such a consistent first-principles framework, however, pioneering aiMD studies of quadrupolar relaxation (see Reference 9 and work by our group 15-18) reported that deviations by a factor of 2 to 3 between calculated and experimental relaxation rates may be difficult to avoid, although extensive multi-trajectory sampling appears to improve the results. Strongly polarizable ions such as iodide continue to pose tremendous challenges in such calculations. For instance, in a pilot study of quadrupolar relaxation from our group, 15 where the sampling was admittedly limited, the calculated relaxation rate for I exceeded the reported experimental rate by a factor of 4. Roberts and Schnitker (RS)³ previously reported calculated quadrupolar relaxation rates of a variety of ions, including ¹³³Cs⁺, ¹²⁷I⁻, and ¹³¹Xe, in aqueous solution that were within roughly a factor of two of the experimental data (with the exception of Mg^{2+}) or better. These calculations used a rigid point-charge model for water in the dynamics, and γ_{∞} Sternheimer factors to treat the solute polarization. The results were deemed 'a remarkable success rate considering the crudity' of the model. It is worth noting that RS pointed out, correctly, that there was a 'considerable uncertainty' in the Sternheimer factor for a given ion. For iodide, for example, RS used $\gamma_{\infty} = -162.42$ from Reference 21. A systematic overestimation for the halide relaxation rates was noted by RS, but their I rate was closer to the experiment than subsequent aiMD-based rates, despite the crude model used for the calculations.

The present work is motivated by the following questions: (i) Can the EFG fluctuations of the aqueous large, polarizable solutes studied herein be calculated accurately and sampled sufficiently from first principles, to obtain accurate quadrupolar relaxation rates? (ii) Can any features of the EFG ACFs for these and other ions be rationalized in terms of specific solvent dynamics in the aiMD? (iii) Do relativistic effects play a significant role in the EFGs and/or relaxation phenomena of these nuclei? (iv) Do the first-principles calculations of the EFG provide insight into the performance of simpler models, in particular those relying on Sternheimer factors?

2 Theoretical and Computational Details

In the limit of fast motion and isotropic conditions, the longitudinal and transverse quadrupolar relaxation rates are equal. We refer to this value as the isotropic rate. This rate can be written as

$$\frac{1}{T_{\rm iso}} = C_Q \langle V(0)^2 \rangle \, \tau_c \tag{1}$$

Here, C_Q is a quadrupolar prefactor containing the quadrupole moment Q and nuclear spin quantum number I of the relaxing nucleus,

$$C_Q = \frac{e^2 Q^2 (2I+3)}{20I^2 (2I-1)\hbar^2}$$
 (2)

and $\langle V(0)^2 \rangle$ is the total EFG variance,

$$\langle V(0)^2 \rangle = \sum_{m} \langle R_{2,m}^*(t) R_{2,m}(t) \rangle \tag{3}$$

in terms of the rank-2 spherical EFG tensor components, $R_{2,m}$, as presented in the formalism of References 25 and 26, for example. Further, τ_c is the characteristic correlation time for the EFG defined here as

$$\tau_c = \frac{1}{\langle V(0)^2 \rangle} \sum_m \int_0^\infty f_{2,m}(\tau) d\tau \tag{4}$$

The integrands $f_{2,m}$ are the ACFs of the EFG tensor components, defined as $f_{2,m}(\tau) = \langle R_{2,m}^*(t)R_{2,m}(t+\tau)\rangle$. The angle brackets indicate an ensemble average. In practice, the ACFs are calculated numerically along the MD trajectories.

Car Parinello aiMD simulations were performed using the Quantum Espresso (QE) package.27 The simulations used a kinetic energy cutoff of 100 Ry for the plane-wave (PW) basis, a fictitious electron mass (μ) of 450 au, and a time step of 6.0 au (0.145 fs). Ultrasoft pseudopotentials based on scalar relativistic calculations were taken from pslibrary 1.0.0.28 Initial, randomized, cell packing consisting of a single analyte atom/ion (Xe, Cs⁺, I⁻), 64 heavy water molecules, and an appropriate counter ion (D⁺/OD⁻) was achieved using the Tinker molecular modeling software package.²⁹ Deuterium was used instead of hydrogen to separate nuclear and electronic degrees of freedom better in the CPMD. The simulation cells were cubic, with a cell parameter of 12.84 Å chosen such that the density of the system was approximately that of pure water at ambient conditions. Five ps of pre-equilibration were performed with Tinker, using NVT force field dynamics. The primary results of this paper are from aiMD simulations utilizing the revised exchange-correlation functional of Perdew, Burke, and Ernzerhof (revPBE). 30-32 Previous studies by us and others^{33,34} showed that the revPBE functional, along with semi-empirical dispersion corrections (D2), 35,36 provides good performance in reproducing solution structure and dynamics, including accurate diffusion coefficients, for aqueous systems, without the need for elevated temperatures. In a previous study, such simulations were used to calculate NMR relaxation via the dipolar mechanism for protons in water and acetonitrile.³⁴ The trajectories for the current study were started from ten PBE simulations for each system at 350 K that we had performed during the early stages of this project (5 ps of NVT equilibration with a three-chain Nosé-Hoover thermostat (90, 45, 15 THz), followed by NVE). The revPBE simulations were re-equilibrated in NVT at 300 K (4.4 ps), followed by production in NVE after 1 ps of further equilibration. Final production times were 25 ps each for Xe and Cs⁺, and 50 ps for Γ . For radial distribution functions (RDFs) and self-diffusion coefficients of the simulated systems compared to experiment, see the supporting information (SI). Good agreement with experiment is seen in the oxygen-oxygen RDFs, and the diffusion coefficients are quite acceptable considering the difficulties of reproducing them from simulations.

For the EFG calculations, clusters of analyte and 30 nearest neighbor solvent molecules were extracted from evenly spaced snapshots of the production phases of the trajectories. Snapshots were taken every 400 frames (0.058 ps), except in the case of Iodide trajectories 1 and 2 for which a 4 times finer sampling (0.0145 ps) was used for testing. Nearest neighbor clustering as well as calculation of RDFs for the periodic systems were done with an open source code developed in our group (version 0.4.1).³⁷ EFGs were computed for the clusters using the Amsterdam Density Functional (ADF) software package (2017 version).³⁸ These calculations employed the hybrid functional PBE0 (25% exact exchange)³⁹ and an all-election Slater-type basis (STO). For the analytes, a quadruple- ζ basis with four sets of polarization functions (QZ4P) was used. A valence double-zeta singly-polarized basis (DZP) was used for solvent atoms. Additional implicit addition of the bulk solvent was included using the Conductor-like Screening Model (COSMO).⁴⁰ EFGs were computed without and with scalar relativistic effects, the latter based on the all-electron Zeroth Order Regular Approximation (ZORA) and picture-change corrections. 41,42 Natural bond orbital (NBO) analyses of the EFGs⁴³ were also carried out for sets of snapshots from one trajectory of each analyte, using the NBO package in ADF (version 6)^{44,45} with the same parameters as above. The following values of Q (taken from reference 46) were used in Equation (2) to generate the relaxation rates: -3.43 mb, -114.6 mb, and -688.22 mb for ¹³³Cs⁺, ¹³¹Xe, and ¹²⁷I⁻ respectively.

3 Results and Discussion

Tables 1, 2, and 3 collect the relaxation rates, correlation times, and $\langle V(0)^2 \rangle$ from the relativistic calculations for all independent trajectories of each system, along with the corresponding means and standard errors. Table 4 summarizes these results, and compares the relativistic and nonrelativistic data with available experimental rates. We note that the experimental relaxation rates of ions in solutions are concentration dependent.^{49–53} The experimental results used here for comparison are those extrapolated to infinite dilution. A first observation is that the calculated and experimental rates are within a factor of 1 to 3 from each other, which was deemed satisfactory in previous—related—aiMD studies of quadrupolar relaxation.^{9,15–17} With multi-trajectory sam-

pling and the fully quantum-mechanical calculations of the EFG tensors, our relaxation rate for $^{127}\text{I}^-$ is markedly improved over the FFMD / Sternheimer model used by RS.³ However, the difference can in large part be attributed to recent revisions of the experimentally determined nuclear quadrupole moment Q for ^{127}I . The most current value of Q for iodide, as reported by Pyykkö, ⁴⁶ and used in this study is $Q_{\text{new}} = -688.2$ mb, whereas RS used a value of $Q_{\text{old}} = -750$ mb. The

Table 1: Summary of ¹³³Cs⁺ relaxation data^a

		·· <i>J</i>			
	$\frac{1}{T_1}$	$\frac{1}{T_2}$	$\frac{1}{T_{\rm iso}}$	$ au_c$	$\langle V(0)^2 \rangle$
1	0.040	0.039	0.040	0.330	0.690
2	0.001	0.008	0.006	0.050	0.680
3	0.061	0.073	0.069	0.629	0.630
4	0.031	0.068	0.056	0.541	0.589
5	0.054	0.027	0.036	0.317	0.651
6	0.036	0.013	0.020	0.173	0.678
7	0.029	0.064	0.052	0.464	0.645
8	0.024	0.023	0.023	0.224	0.596
9	0.004	0.011	0.008	0.078	0.617
10	0.020	0.021	0.020	0.178	0.659
Average	0.030	0.035	0.033	0.298	0.644
St.Err	0.006	0.007	0.006	0.059	0.011

^afrom ten 25 ps aiMD simulations and relativistic STO/PBE0 EFG calculations. $\langle V(0)^2 \rangle$ in au. Trajectories sample snapshots every 0.058 ps.

Table 2: Summary of ¹³¹Xe relaxation data^a

	$\frac{1}{T_1}$	$\frac{1}{T_2}$	$\frac{1}{T_{\mathrm{iso}}}$	$ au_c$	$\langle V(0)^2 \rangle$
1	76.6	69.0	71.5	0.134	0.281
2	91.7	76.7	81.7	0.171	0.250
3	80.1	47.2	58.2	0.114	0.266
4	110.4	148.0	135.5	0.286	0.249
5	143.9	130.0	134.6	0.298	0.237
6	239.4	105.8	150.3	0.410	0.192
7	148.6	185.7	173.4	0.363	0.251
8	142.0	57.1	85.4	0.173	0.258
9	12.9	4.9	7.6	0.016	0.242
10	20.2	85.4	63.7	0.162	0.207
Average	106.6	91.0	96.2	0.213	0.243
St.Err	20.0	15.9	15.2	0.037	0.008

^afrom ten 25 ps aiMD simulations and relativistic STO/PBE0 EFG calculations. $\langle V(0)^2 \rangle$ in au. Trajectories sample snapshots every 0.058 ps.

relaxation rates scale with Q^2 , so the effect of including the updated quadrupole moment is a decrease in the computed rate by a factor of $Q_{\text{new}}^2/Q_{\text{old}}^2 = 0.84$. Our computed rates for $^{133}\text{Cs}^+$ and ^{127}Xe are comparable or worse to those of RS. Indeed, an important source of error is the quality of intermolecular potentials which can be obtained from aiMD with DFT+D2, and there are, of course, the ubiquitous issues of incomplete sampling and the limited sizes of the simulation cells. The finite-cluster EFG calculations approximate the embedding of the ions further. On the positive side, it is known that DFT calculations typically perform well for EFGs in main group atoms. $^{43,54-56}$

Table 3: Summary of calculated ¹²⁷I⁻ relaxation data^a

	$\frac{1}{T_1}$	$\frac{1}{T_2}$	$\frac{1}{T_{\rm iso}}$	$ au_c$	$\langle V(0)^2 \rangle$
1	6891	11886	10221	0.490	1.263
2	8620	3562	5248	0.277	1.147
3	9156	10163	9827	0.416	1.432
4	10024	3416	5619	0.283	1.203
5	9112	16697	14169	0.556	1.542
6	984	764	837	0.046	1.104
7	3526	1919	2455	0.127	1.174
8	5560	3366	4097	0.219	1.132
9	3898	3846	3863	0.199	1.176
10	18729	19545	19273	1.006	1.160
Average	7650	7517	7561	0.362	1.233
St.Err	1464	1988	1730	0.083	0.043

^a from ten 50 ps aiMD simulations and relativistic STO/PBE0 EFG calculations. $\langle V(0)^2 \rangle$ in au. Trajectories 1-2 sample snapshots every 0.0145 ps and trajectories 3-10 sample snapshots every 0.058 ps.

Table 4: Summary of mean relaxation data^a from sets of ten simulations of each system

System	$\langle V(0)^2 \rangle$	τ_c (ps)	$\frac{1}{T_{\rm iso}} (\mathrm{s}^{-1})$	$\frac{1}{T_{1,\exp}} (s^{-1})^b$
133Cs ⁺ (nrel)	0.50(1)	0.30(6)	$26(5) \cdot 10^{-3}$	$75\cdot 10^{-3}$
			$33(6) \cdot 10^{-3}$	-
¹³¹ Xe (nrel)				179
¹³¹ Xe (rel)	0.24(1)	0.21(4)	96(15)	-
¹²⁷ I ⁻ (nrel)	0.94(3)	0.36(8)	$57(12) \cdot 10^2$	$46 \cdot 10^2$
¹²⁷ I ⁻ (rel)	1.23(4)	0.36(8)	$76(16)\cdot 10^2$	-

^a Relativistic and nonrelativistic STO/PBE0 EFG calculations. Results are rounded to two significant figures and standard errors are provided in parentheses. $\langle V(0)^2 \rangle$ in au. ^bFrom references 47 (¹³³Cs⁺ and ¹²⁷I⁻;), and 48 (¹³¹Xe); Exptl. results are at $T=25^{\circ}$ C

As mentioned in the Introduction, RS acknowledged the crude approximations made in their computations, in particular in the EFG calculations. The references given in RS for the Sternheimer factors^{21,57} report large uncertainties for γ_{∞} . The values for ¹³³Cs⁺ (-110.81) and ¹²⁷I⁻ (-162.42) were computed²¹ using a 'Watson sphere' model in which the ion is surrounded by a sphere of opposite charge at a fixed distance, to model the ion in a solid. The reference⁵⁷ given for γ_{∞} for Xe reports an experimentally derived value of -157, but notes large uncertainties. For iodide especially, the Watson sphere effects had a profound effect on the calculated γ_{∞} , decreasing its magnitude from -299 to -162. Since the relaxation rate scales with $(1 + \gamma_{\infty})^2$, this has a very large effect on the computed rates. In the study of RS, this rough correction to the calculated free ion γ_{∞} therefore dramatically improves the relaxation rate for iodide with respect to experiment.

The relative standard errors, which are rough estimates of the true sampling errors, in the computed relaxation rates are 18%, 15%, and 22% for ¹³³Cs⁺, ¹³¹Xe, and ¹²⁷I⁻, respectively. The variations in the correlation times τ_c between different trajectories are primarily responsible for the standard errors. In comparison, $\langle V(0)^2 \rangle$ is more consistent across the trajectories, especially for Cs⁺. Average EFG ACFs for the three systems are shown in Figure 1, and the running integrals of the EFG ACFs for each trajectory are shown in Figure 2. The running integrals are of the isotropic EFG ACF, taken here to be the mean of all second-rank spherical components, $f_{2,m}(\tau)$, for a given trajectory. Although the the average EFG ACFs and those of all individual trajectories (see supporting information) appear well converged on a sub-ten picosecond time scale, in Figure 2, it can be seen that long-time (greater than 10 ps) correlations and anti-correlations can cause great variations influencing the spectral densities for individual trajectories. If the lower outlier trajectory for ¹³¹Xe (trajectory 9 in Table 2) and the upper outlier for ¹²⁷I⁻ (trajectory 10 in Table 3) which can be seen in Figure 2b-c are excluded, the mean relaxation rate becomes 106 Hz for ¹³¹Xe and 6260 Hz for ¹²⁷I⁻ in the relativistic case. These are well within a factor of 2 of the experimental value and much improved over previously computed rates.^{3,58} The long-time contributions to the spectral density that result in such outliers may be a result of slow or rare dynamic events that are incompletely sampled in the aiMD simulations (which, however, are of relatively long duration for these types of simulations, especially for I⁻). One such type of event could be solvent molecule escape dynamics from the hydration shell, which was shown in aiMD studies to have time constants of up to 16 ps for aqueous iodide. 59-62 These considerations motivated the increased simulation times for aqueous iodide.

As far as the averaged EFG ACFs in Figure 1 are concerned, as established in the literature for these and other systems,^{3,13,14,16} a two-step decay process can be seen. An initial steep decay in the first fraction of a picosecond (libration region) is followed by a slower decay that accounts for most of the correlation time. A unique feature can be seen in the ACF for the I⁻ simulations, in the form of a small oscillation or 'notch' in the transition between the two decay regimes. In

previous work, ¹⁶ and that of others, ^{2,14} a similar 'notch' feature can be seen in the EFG ACFs of CI⁻, however, an explanation was not provided. In the dynamics literature, there are examples of a similar feature at the same time scale in the linear velocity and rotational ACFs of pure water^{7,10,63-65} as well as for water molecules in the first hydration sphere of small ions. ^{2,8} The oscillation is generally attributed to the oscillatory nature of the vibrational and librational motion of the water molecule in its hydrogen bond network. Figure 3 shows our calculated rotational ACFs of the first solvent shell water molecules surrounding each of the ions. The 'notch' is present for all three systems. For anions, however, the coordinated water molecules have their O-H (O-D in this case) bond vector pointed towards the anion. Libration of these water molecules is characterized by angular oscillations of the O-D bond vector, in which the heavier oxygen nucleus is relatively stationary and the deuteron undergoes oscillatory motion, drawing out a 'cone of libration' with its range of motion. This libration, with the partial positive end of the O-D bond dipole pointed towards the anion is more likely to induce a corresponding response in the fluctuations of the EFG of the polarizable anion.

Compared to the correlation times, $\langle V(0)^2 \rangle$ has significantly less scatter across the sets of independent trajectories. The analogous quantity reported by RS does not contain the $(1+\gamma_\infty)^2$ factor for the contributions of the ion polarization to the EFG. After multiplying with this factor, the RS values for $\langle V(0)^2 \rangle$ are 0.268, 0.258, and 0.966 au for Cs⁺, Xe, and Γ , respectively. Our relativistic Xe and nonrelativistic Γ values for $\langle V(0)^2 \rangle$ have comparable magnitudes. The Cs⁺ value of RS seems low, when compared to Xe, given that—unlike Xe—there are strong ion-dipole interactions between Cs⁺ and the solvent. Despite the comparatively small $\langle V(0)^2 \rangle$, the RS relaxation rate for Cs⁺ is 0.042 s⁻¹, slightly larger than ours, because RS determined a τ_c of 0.64 \pm 0.16 ps which is about twice ours. The RS correlation times for Xe and Γ are comparable to ours.

In terms of relativistic effects on the computed EFGs, it can be seen in Table 4 that there is a systematic increase of $\langle V(0)^2 \rangle$ by a factor of about 1.3 from scalar relativistic effects in the three systems. This means that on average the EFGs are enhanced by about 14%. Available small-molecule benchmark data, for example in Reference 24, show that a 14% increase due to scalar relativistic effects is quite typical for iodine EFGs. Data from the same reference also show that relativistic effects on iodine EFGs from spin-orbit coupling (SOC) are an order of magnitude smaller than the scalar relativistic effects. We therefore neglected the SOC in the present study, to keep the computational cost more manageable. Figure 4 plots the comparison of the computed relativistic and nonrelativistic V_{zz} for a large set of trajectory snapshots. While the systems span different magnitudes of the field gradient, the slopes of the resulting correlation lines are similar, and there is essentially no scatter. (The comparison of relativistic vs. nonrelativistic calculations is for the EFG only, not for the underlying aiMD trajectories which were consistently carried out

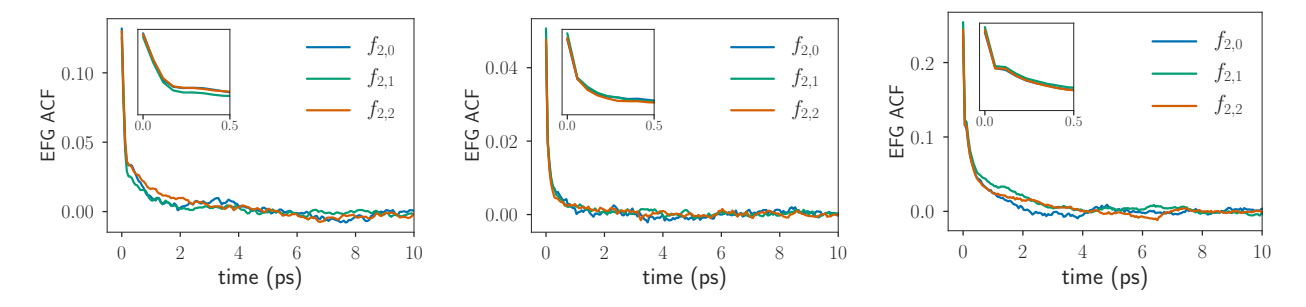


Figure 1: ACFs of the spherical EFG tensor components. Left: ¹³³Cs⁺, Middle: ¹³¹Xe, Right: ¹²⁷I⁻. Inset shows behavior of the ACF in the first 0.5 ps.

with relativistic pseudopotentials.) For ¹³³Cs⁺ and ¹³¹Xe, the resulting increases in the relaxation rates due to relativistic effects constitute improvements with respect to experiment, whereas for ¹²⁷I⁻ the overestimation of the rate by the calculations is worsened, thereby exposing the presence of error cancellation in the nonrelativistic relaxation rate.

A detailed analysis (vide infra) shows that the EFGs, and the substantial relativistic effects thereupon, are generated predominantly in the valence and outer core shells of the solute. This is expected, because the EFG operator has an inverse cubic dependence on the distance from the solute nucleus, and the relativistic effects generated by the solvent nuclear charges are negligible compared to those generated by the high solute nuclear charges. In this context, it is interesting that the relativistic effects on the correlation times τ_c are negligible (Table 4). From Equation (4) it is clear that there must be a near-complete cancellation of the relativistic effects in the numerator and the $\langle V(0)^2 \rangle$ denominator, indicating that the relativistic effects can be factored out of the integrals over $f_{2,m}$, approximately, such that they hardly influence the EFG autocorrelation. This is consistent with Figure 4 which makes clear that relativistic effects have a simple linear scaling effect on the total EFG, with virtually no scatter among the different configurations. Relativistic effects scale the magnitude of the EFG induced by polarization of the solute orbitals, but have no effect on its 'memory' of previous values as the solvent environment evolves in time. This need not hold true generally, however. If a greater degree of scatter, or some nonlinear relationship in Figure 4 were observed, it would be possible for the relativistic and nonrelativistic τ_c to disagree. In Equation (1), the full $\langle V(0)^2 \rangle$ must be used, which is massively amplified over the corresponding value determined from the external partial charges only, due to solute polarization and close-contact interactions with the solvent. The lack of relativistic effects on τ_c is therefore an indicator for why a crude approximation such as scaling the external EFG with a constant to obtain the full $\langle V(0)^2 \rangle$ does not fail completely in relaxation rate calculations, as long as $(1 + \gamma_{\infty})$ is chosen judiciously.

To gain further insight into the EFGs entering $\langle V(0)^2 \rangle$ and the correlation times, we performed

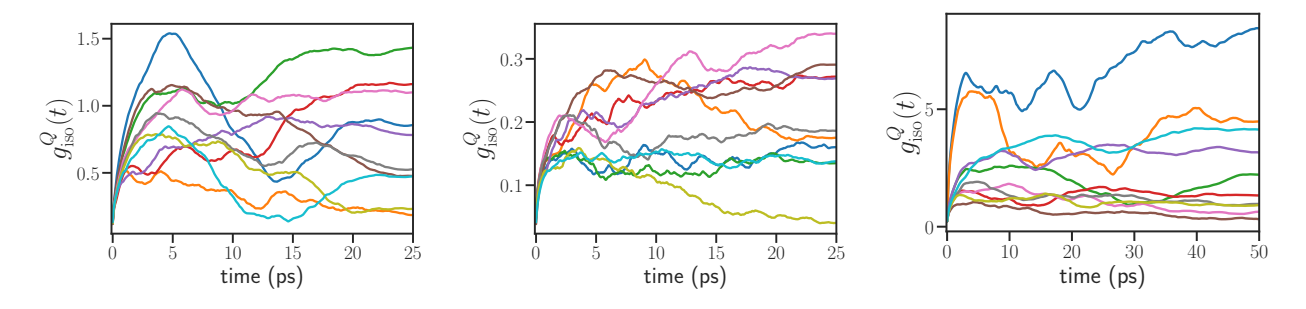


Figure 2: Running integrals (denoted $g_{iso}(\omega, t)$) of the isotropic EFG ACFs for each independent trajectory. Left: ¹³³Cs⁺, Middle: ¹³¹Xe, Right: ¹²⁷I⁻

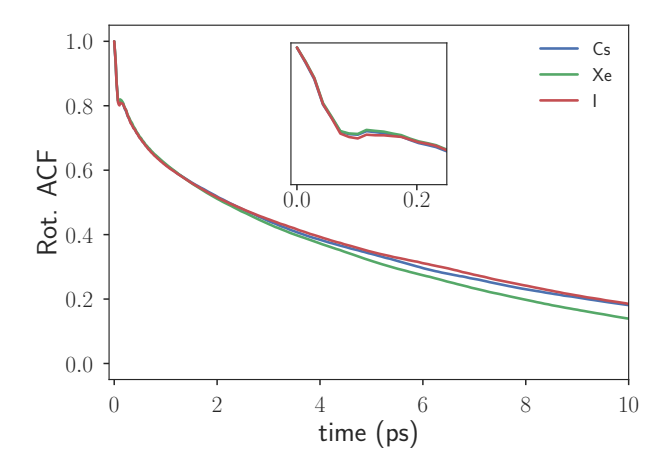


Figure 3: Rotational ACFs for water molecules in the first solvation shell of each system, averaged across independent trajectories. Inset shows the behavior of the ACF in the first 0.25 ps.

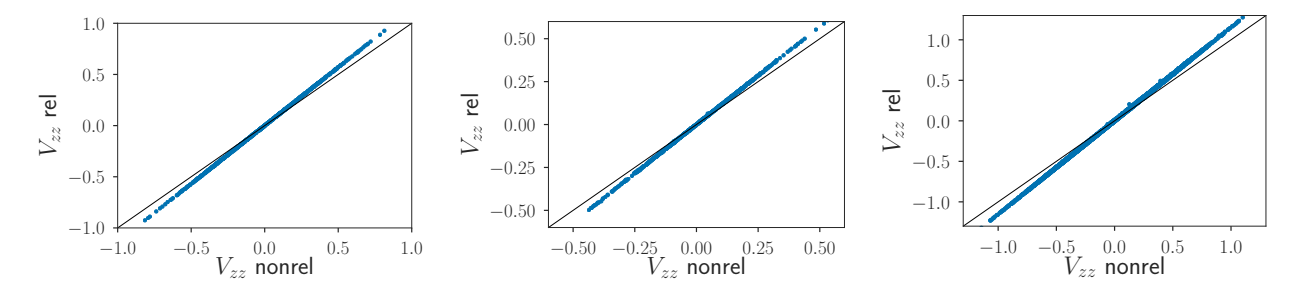


Figure 4: Comparison of V_{zz} EFG component (in au) calculated with (rel) and without scalar relativistic corrections (nonrel). Scattered points each represent a different configuration along the trajectories. y = x is plotted for comparison. Left: ¹³³Cs⁺, Middle: ¹³¹Xe, Right: ¹²⁷I⁻

an analysis in terms of localized orbitals. The procedure is detailed in Reference 43. Specifically, we used the natural bond orbitals (NBOs) and natural localized molecular orbitals (NLMOs) generated by the NBO algorithms. ⁴⁵ The EFG tensor component V_{uv} , with $u, v \in \{x, y, z\}$ chosen to coincide with the EFG principal axis system, at a nucleus located at \mathbf{R}_A is given in atomic units

by

$$V_{uv} = \int \rho(\mathbf{r}) \left[\hat{V}_{uv}(\mathbf{r}, \mathbf{R}_A) - \frac{1}{N} \sum_{B \neq A}^{\text{Nuclei}} Z_B \hat{V}_{uv}(\mathbf{R}_B, \mathbf{R}_A) \right] dV$$
 (5)

Here, $\hat{V}_{uv}(\boldsymbol{p},\boldsymbol{q}) = \delta_{uv}|\boldsymbol{p}-\boldsymbol{q}|^{-3} - 3(p_u - q_u)(p_v - q_v)|\boldsymbol{p}-\boldsymbol{q}|^{-5}$ is the traceless quadrupole operator, N is the number of electrons, and Z_B the charge of another nucleus. In the analysis,

Table 5: NLMO/NBO contributions to most positive EFG tensor principal component V_+ , averaged over one trajectory per system^a

	Cs	Xe	I
NLMO rel.			
$core^b$	0.1344	0.0285	0.0620
Σ 5s,5p	0.2539	0.3050	0.6641
other ^c	0.1907	0.0097	-0.0110
total ^d	0.5790	0.3432	0.7152
NLMO nrel.			
$core^b$	0.1199	0.0239	0.0553
Σ 5s,5p	0.2237	0.2692	0.5754
other ^c	0.1681	0.0076	-0.0093
total ^d	0.5117	0.3007	0.6214
NBO rel.			
$core^b$	0.0658	0.0143	0.0329
Σ 5s,5p	0.1257	0.2755	0.3219
$diffuse^f$	0.1197	0.0047	0.0262
other ^c	0.2677	0.0487	0.3342
total ^d	0.5790	0.3432	0.7152
NBO nrel.			
$core^b$	0.0588	0.0114	0.0296
Σ 5s,5p	0.1120	0.1709	0.2377
$diffuse^f$	0.1505	0.0138	0.0121
other ^c	0.1904	0.1045	0.3421
total ^d	0.5117	0.3007	0.6214

^aAverages of the most positive principal component of the EFG (in atomic units) in each trajectory snapshot, as opposed to the principal component V_{33} , defined as the largest-magnitude component. One trajectory is sampled for each system (Cs⁺: traj. 1, Xe: traj. 1, and Γ: traj. 2, with respect to the trajectory numbering in Tables 1-3). Numbers of snapshots averaged for each system are Cs⁺: 433, Xe: 432, and Γ: 479. ^bSum of contributions from core orbitals (n < 5) centered on the solute. ^cSum of contributions from NLMOs/NBOs centered on solvent atoms. ^fSum of contributions from solute-centered diffuse ('Rydberg') NBOs. ^dSum of all NLMO/NBO contributions in a given set of calculations, equivalent to the total calculated V_+ average.

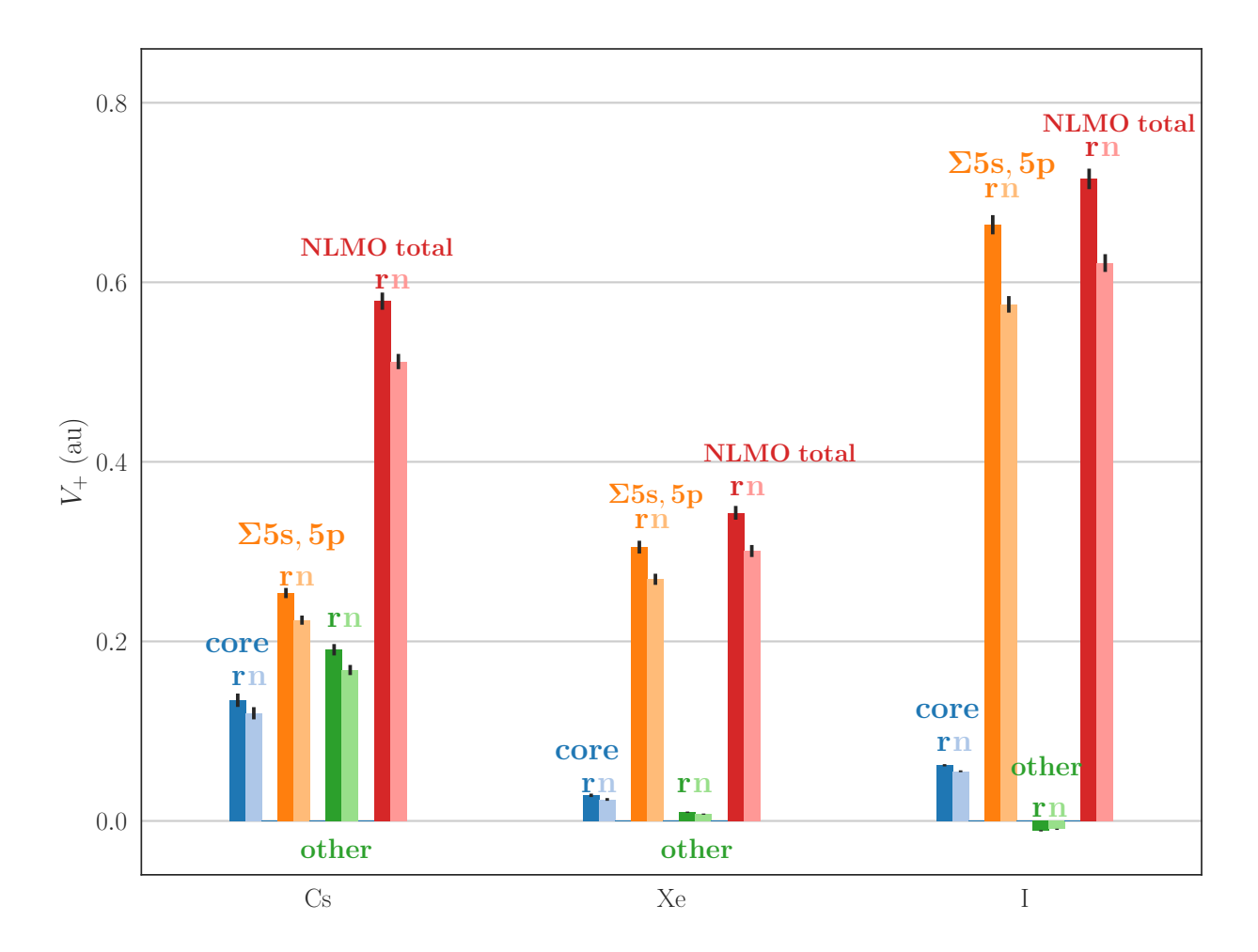


Figure 5: Mean NLMO contributions to the most positive principal component of the EFG, V_+ . Relativistic (r) versus nonrelativistic (n) EFG calculations. Error bars represent the standard error in the mean. Labels are defined in the caption of Table 5.

the electron density $\rho(\mathbf{r})$ is partitioned into orbital densities, thus providing a contribution to the EFG from each individual localized orbital. The contributions to the EFG from other nuclear charges are weighted by the electron density, as shown above, and thereby absorbed into the analysis. It is worthwhile pointing out that a breakdown of a quantum mechanical observable into contributions from individual orbitals is not unique. However, the NBO/NLMO analysis, in terms of 'chemist's' orbitals, is particularly intuitive. Namely, the NBOs represent ideally localized lone pairs, bonds, or core shells, with associated integer or non-integer electron populations. Each NLMO is doubly occupied (for closed-shell systems) and has a closely related 'parent' NBO. The NLMOs may be delocalized, relative to their parent NBOs, to reflect the electron delocalization in the system. In this context, it is important to note that donation bonding is a form of electron delocalization that may be represented by a lone pair NBO with a pronounced 'delocalization tail' in the corresponding NLMO.

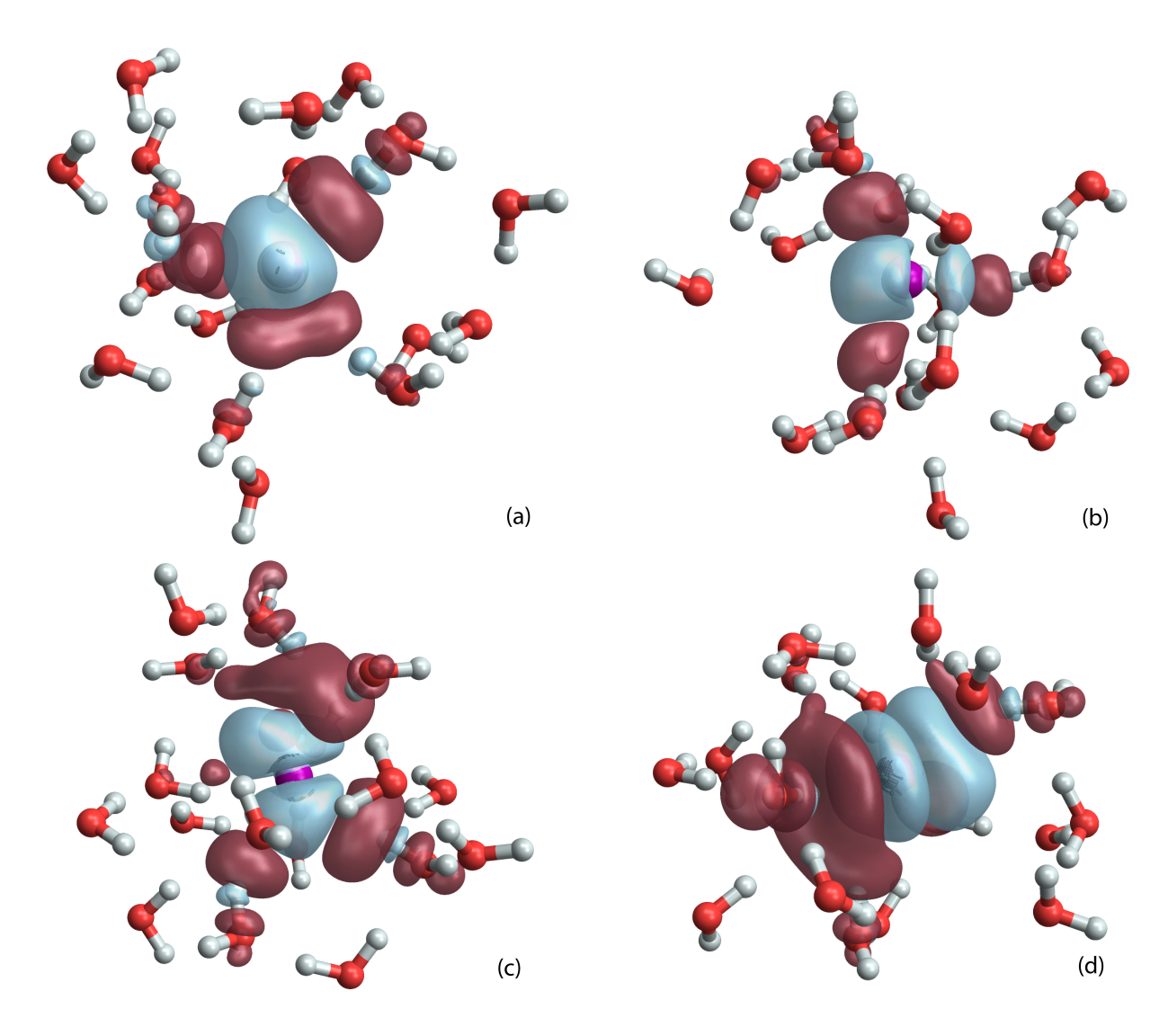


Figure 6: Difference isosurfaces (red/gray isovalues = $\pm 1 \times 10^{-4}$) of NLMO minus NBO densities for (a) 5s and (b-d) 5p orbitals from a representative iodide trajectory snapshot with $V_+ = 1.44$ au.

Table 5 provides a summary of the analysis. A visual breakdown of the NLMO analysis, with error bars, is provided in Figure 5. For each system, between 400 and 500 configurations from one of the trajectories were subjected to the analysis. Because the sign of V_{33} fluctuates, the data in Table 5 represent the trajectory averages of the most positive EFG principal component, denoted here as V_+ . The orbital contributions are grouped into those from the [Kr]4d¹⁰ cores, the 5sp shells, diffuse NBOs that are centered on the solute, and the sum of all other contributions. The solute valence shell and core shell polarization are associated with the 5sp and core contributions. The 'diffuse' category appears only in the analysis by NBOs. Here, we sought to distinguish, qualitatively, between solute-centered atomic contributions versus solvent-centered contributions due to the NLMO delocalization. The direct contributions of solvent partial charges to the solute

EFG, constituting the external EFG, show up in Table 5 mainly in the 'other' category. It should be noted, however, that—in particular in the NBO partitioning—the 'other' category also includes the aforementioned delocalization tails that may appear, for instance, due to steric and partially covalent interactions between the solute and solvent.

By taking the ratio of the total V_+ over the 'other' contributions for a given system, we obtain a scaling factor for the external EFG analogous to the Sternheimer antishielding factor used in models where the solute polarization contributions are not treated explicitly. For Xe, the NLMO analyses yield a ratio 35 and 40 in the relativistic and nonrelativistic calculations, respectively. These values are far below the magnitude of $1 + \gamma_{\infty}$ for Xe and have the opposite sign, given that the aforementioned $\gamma_{\infty} = -157$ is negative (although this does not matter in the relaxation rate calculation when $|\gamma_{\infty}| \gg 1$). Table S4 in the supporting information shows that 5s and 5p contributions to the averaged V_+ are of opposite sign; and for an external EFG ('other') that is on average positive, the contributions from 5p is negative on average. However, the breakdown of the contributions into 5s vs. 5p is not clean, and therefore absent from Table 5, because for many of the MD configurations the 5sp NBOs are strongly hybridized. Moreover, the 5s orbital must acquire considerable 5p character through polarization or hybridization to produce a significant EFG on it own. For Γ , the external ('other') EFG is negative, on average, for the most positive EFG component along the trajectory, and here the ratio of the total and external EFG is -65. For Cs⁺, the ratio is +3.

In the NLMO analysis, the relativistic effects on V_{+} are almost entirely associated directly with the 5sp shell and the concomitant polarization of the (outer) core shells. In the NBO analysis, a strong increase in the 5sp contributions due to relativistic effects is accompanied by a decrease in the 'other' contributions for Xe, and an increase for Cs⁺, which gives a strong hint that most of the 'other' contributions in the NBO analysis should indeed be associated with the 5sp shell and the delocalization tails of solvent-centered NLMOs, rather than the surrounding water molecules. For Cs⁺, the 'other' contribution in the NLMO analysis, and the relativistic effects thereupon, are particularly large in absolute terms. This means the oxygen lone pair orbitals of the coordinating water molecules must be hybridized with empty Cs valence orbitals, in particular 6sp. Indeed, the calculations show a non-negligible sum occupation of the 6sp NBOs for Cs⁺, with an average of ca. 0.05 electrons along the probed trajectory, which is roughly five times larger than the average sum of 6s and 6p NBO occupations of Xe and I⁻. (3s NBO occupations between 0.1 and 0.2 were recently reported by us for Na⁺ encapsulated in a cryptand. 18) The Cs⁺ 6s shell undergoes a relativistic contraction, and it hybridizes/polarizes in the presence of an asymmetric solvent coordination motif, which rationalizes the relativistic effects in the 'other' NLMO contributions in the EFG. There is evidently a degree of oxygen-cesium donation bonding present, which influences the EFG and is subject to relativistic effects. The water molecules

are therefore hardly to be considered 'external' when it comes to the EFG, which explains the smallest other/total ratio of three mentioned in the previous paragraph. Nonetheless, as already mentioned, the water dynamics determines τ_c , with the relativistic effects on the EFG, in part from the O–Cs interactions, mainly leading to a very similar increase of the numerator and the denominator in Equation (4).

The changes in the 'other' contributions between the NLMO and NBO analyses are particularly large for Γ . Figure 6 shows the differences in the electron density contributions from the 5s and 5p NLMOs versus NBOs. The density difference is clearly in the diffuse region around iodide, with contributions on the nearest water molecules likely to be attributable mainly to the orthogonality of the NLMOs on the water orbitals, i.e., steric effects. Given that this anion is particularly strongly polarizable, it makes sense that the 5sp NBOs are not sufficient to describe the EFG induced by electrostatic polarization and other effects from the surrounding solvent molecules. When the diffuse region around Γ is absorbed into the ion contribution, in the NLMO description, this results in an 'other' contribution versus total EFG in the analysis that most closely resembles the Sternheimer correction used by RS.

4 Summary, Conclusions, and Outlook

NMR relaxation rates for the heavy, quadrupolar species ¹²⁷ I⁻, ¹³¹ Xe, and ¹³³ Cs⁺ in water were computed via aiMD simulations and subsequent cluster calculations of the EFG tensor at the KS hybrid DFT level. In keeping with previous work, sets of ten independent trajectories were developed for each system, providing improved sampling over single-trajectory MD and access to statistical errors in the computed rates. We have also investigated the effects of scalar relativistic corrections on the EFGs at these heavy nuclei, and the concomitant effects on the relaxation rates. The DFT framework used for the EFGs also allowed for a deeper analysis of their origins, and for an assessment of the validity of the Sternheimer approximation for these large, polarizable, atomic species. An analysis of contributions to the EFG at each analyte nuclei in terms of localized orbitals was performed to give a first principles perspective on the external versus core polarization contributions to the EFG.

In light of our results, we now address the motivating questions posed in the Introduction. (i) Our methods result in relaxation rates within a factor of one to three of the experiments and highlight the challenge of performing consistently better in a fully first-principles approach. For ¹²⁷I⁻, the result is much improved over our previous aiMD-based approach, which had poor sampling. ¹⁵ Compared to previous strong over-estimations of the iodide quadrupolar relaxation rates, there is also a significant improvement from recent updates ⁴⁶ to the measured nuclear quadrupole moment for ¹²⁷I. Between the quality of the forces obtained in the dynamics, the degree of sampling

achieved, accuracy of experimentally determined constants (i.e. Q), and validity of Sternheimer factors in the formalism of RS, clearly there are many variables which enter into the computation of the relaxation rates between the two studies. This makes the overall agreement between our results and those of RS all-the-more surprising. However some significant differences with RS are nonetheless obtained. For example, for $^{133}\text{Cs}^+$, our computed $\langle V(0)^2 \rangle$ is significantly greater than that of RS, being counterbalanced by τ_c which is lower than that of RS by a similar factor, leading to a comparable relaxation rate. (ii) A dynamic mechanism explains the 'notch' feature of the EFG ACF of halides in water. Rotational ACFs of water in the first solvation shell suggest that large-amplitude hydrogen libration causes a characteristic oscillation in the EFG ACF of negatively charged ions. (iii) Relativistic effects are shown to increase $\langle V(0)^2 \rangle$ considerably, but they have virtually no effect on τ_c . The relativistic increase in $\langle V(0)^2 \rangle$ leads to a proportional increase in the relaxation rates. This effect is corrective with respect to the agreement between calculations and experiments for ¹³³Cs⁺ and ¹³¹Xe, but it causes a greater overestimation of the ¹²⁷I⁻ rate. (iv) An analogue to the Sternheimer polarization factor was estimated based on the NLMO decomposition of the EFG. Only the value for iodide resembles the corresponding γ_{∞} qualitatively, and all of them are much lower in magnitude than the γ_{∞} values used by RS. From a first principles perspective, the line is blurred between 'internal' and 'external' contributions to the electron density and the associated EFG. Diffuse solute-centered contributions in the NLMO picture, are associated with the solvent in the NBO picture. For the most polarizable of the solutes, in iodide, this results in a significant difference in the effective external EFG contribution in the two analyses (NBO vs. NLMO). On the other hand, Cs⁺ displays a large external EFG contribution in the NLMOs and evidence was found for electron donation of solvent into the cesium 6sp orbitals. To our knowledge, this is the first fully ab-initio NMR relaxation study of these polarizable 'relativistic' solutes. We believe this investigation opens the door to more widespread applications of first-principles approaches to interpret and predict condensed-phase NMR relaxation rates.

Acknowledgments

We acknowledge the Center for Computational Research (CCR) at the University at Buffalo for providing computational resources, in particular those made available via grant MRI-1724891 from the National Science Foundation (NSF). This work has been supported by NSF grant CHE-1855470.

Supporting Information Available

Full nonrelativistic relaxation data for all trajectories of each system. EFG ACFs of all individual trajectories. Oxygen-oxygen RDFs and diffusion constants compared to experimental heavy water. X-Oxygen and X-Hydrogen RDFs (X=Cs,Xe,I). Iodide coordination number distributions. Comparison of EFGs computed with hybrid and non-hybrid functionals. Comparison of EFGs computed with TZ2P versus QZ4P basis. Cartesian EFG components along with distance of nearest neighbor solvent atom to the solute, plotted versus simulation time. Separated 5s and 5p NBO/NLMO contributions to EFG. Bar plot of average NBO contributions to EFG. Isosurfaces of the solute-centered 5s NLMO in a representative snapshot of each system. This material is available free of charge via the Internet at http://pubs.acs.org.

References

- [1] Engström, S.; Jönsson, B.; Bengt, J. A molecular approach to quadrupole relaxation. Monte Carlo simulations of dilute Li⁺, Na⁺, and Cl⁻ aqueous solutions. *J. Magn. Reson.* **1982**, *50*, 1–20.
- [2] Engström, S.; Jönsson, B. Molecular dynamic simulation of quadrupole relaxation of atomic ions in aqueous solution. *J. Chem. Phys.* **1984**, *80*, 5481–5486.
- [3] Roberts, J. E.; Schnitker, J. Ionic quadrupolar relaxation in aqueous solution: dynamics of the hydration sphere. *J. Phys. Chem.* **1993**, *97*, 5410–5417.
- [4] Odelius, M. Molecular Dynamics Simulations of Quadrupolar Relaxation of ¹³¹Xe in Methanol. An Ellipsoidal Picture of the Electric Field Gradient Tensor. *J. Phys. Chem.* **1994**, 98, 12108–12116.
- [5] Odelius, M.; Holz, M.; Laaksonen, A. Quadrupolar Relaxation of ²¹Ne, ⁸³Kr, and ¹³¹Xe Dissolved in Acetonitrile. A Molecular Dynamics Study. *J. Phys. Chem. A* **1997**, *101*, 9537–9544.
- [6] Perng, B.-C.; Ladanyi, B. M. A dielectric theory of spin-lattice relaxation for nuclei with electric quadrupole moments. *J. Chem. Phys.* **1998**, *109*, 676–684.
- [7] Laage, D.; Hynes, J. T. Do more strongly hydrogen-bonded water molecules reorient more slowly?. *Chem. Phys. Lett.* **2006**, *433*, 80–85.
- [8] Laage, D.; Hynes, J. T. Reorientional dynamics of water molecules in anionic hydration shells. *Proc. Acad. Natl. Sci.* **2007**, *104*, 11167–11172.

- [9] Schmidt, J.; Hutter, J.; Spiess, H.-W.; Sebastiani, D. Beyond Isotropic Tumbling Models: Nuclear Spin Relaxation in Liquids from First Principles. *ChemPhysChem* **2008**, *9*, 2313–2316.
- [10] Laage, D.; Hynes, J. T. On the Molecular Mechanism of Water Reorientation. *J. Phys. Chem. B* **2008**, *112*, 14230–14242.
- [11] Stirnemann, G.; Wernersson, E.; Jungwirth, P.; Laage, D. Mechanisms of Acceleration and Retardation of Water Dynamics by Ions. *J. Am. Chem. Soc.* **2013**, *135*, 11824–11831.
- [12] Aidas, K.; Ågren, H.; Kongsted, J.; Laaksonen, A.; Mocci, F. A quantum mechanics/molecular dynamics study of electric field gradient fluctuations in the liquid phase. The case of Na⁺ in aqueous solution. *Phys. Chem. Chem. Phys.* **2013**, *15*, 1621–31.
- [13] Carof, A.; Salanne, M.; Charpentier, T.; Rotenberg, B. Accurate Quadrupolar NMR Relaxation Rates of Aqueous Cations from Classical Molecular Dynamics. *J. Phys. Chem. B* **2014**, *118*, 13252–13257.
- [14] Carof, A.; Salanne, M.; Charpentier, T.; Rotenberg, B. On the microscopic fluctuations driving the NMR relaxation of quadrupolar ions in water. *J. Chem. Phys.* **2015**, *143*, 194504.
- [15] Badu, S.; Truflandier, L. A.; Autschbach, J. Quadrupolar NMR Spin Relaxation Calculated Using Ab-initio Molecular Dynamics: Group 1 and Group 17 Ions in Aqueous Solution. *J. Chem. Theory Comput.* **2013**, *9*, 4074–4086.
- [16] Philips, A.; Marchenko, A.; Truflandier, L. A.; Autschbach, J. Quadrupolar NMR relaxation from ab-initio molecular dynamics: Improved sampling and cluster models vs. periodic calculations. *J. Chem. Theory Comput.* **2017**, *13*, 4397–4409.
- [17] Philips, A.; Marchenko, A.; Ducati, L. C.; Autschbach, J. Quadrupolar ¹⁴N NMR Relaxation from Force-Field and Ab-Initio Molecular Dynamics in Different Solvents. *J. Chem. Theory Comput.* **2019**, *15*, 509–519.
- [18] Abella, L.; Philips, A.; Autschbach, J. The sodium anion is strongly perturbed in the condensed phase even though it appears like a free ion in NMR experiments. *J. Phys. Chem. Lett.* **2020**, *11*, 843–850.
- [19] Sternheimer, R. On Nuclear Quadrupole Moments. Phys. Rev. 1950, 80, 102–103.
- [20] Sternheimer, R. M. Quadrupole Shielding and Antishielding Factors for Several Atomic Ground States. *Phys. Rev. A* **1972**, *6*, 1702–1709.

- [21] Schmidt, P. C.; Sen, K. D.; Das, T. P.; Weiss, A. Effect of self-consistency and crystalline potential in the solid state on nuclear quadrupole Sternheimer antishielding factors in closed-shell ions. *Phys. Rev. B* **1980**, *22*, 4167–4179.
- [22] Pyykkö, P. Relativistic Effects in Chemistry: More Common Than You Thought. *Annu. Rev. Phys. Chem.* **2012**, *63*, 45–64.
- [23] Autschbach, J. Perspective: Relativistic Effects. J. Chem. Phys. 2012, 136, 150902.
- [24] Aquino, F.; Govind, N.; Autschbach, J. Electric field gradients calculated from two-component relativistic density functional theory including spin-orbit coupling. *J. Chem. Theory Comput.* **2010**, *6*, 2669–2686.
- [25] Spiess, H. W. Rotation of Molecules and Nuclear Spin Relaxation. In *NMR Basic Principles and Progress*, Vol. 15; P. Diehl, R. K. E. Fluck, Ed.; Springer: Berlin, 1978 55–214.
- [26] Cowan, B. *Nuclear Magnetic Resonance and Relaxation;* Cambridge University Press: Cambridge, UK, 2005.
- [27] Giannozzi, P.; Baroni, S.; Bonini, N.; Calandra, M.; Car, R.; Cavazzoni, C.; Ceresoli, D.; Chiarotti, G. L.; Cococcioni, M.; Dabo, I. *et al.* QUANTUM ESPRESSO: a modular and open-source software project for quantum simulations of materials. *J. Phys. Cond. Mat.* **2009**, *21*, 395502.
- [28] Dal Corso, A. Pseudopotentials periodic table: From H to Pu. *Comput. Mater. Sci.* **2014**, *95*, 337–350.
- [29] TINKER Software Tools for Molecular Design by J. W. Ponder. URL https://dasher.wustl.edu/tinker/. Accessed 09/18.
- [30] Perdew, J. P.; Burke, K.; Ernzerhof, M. Generalized Gradient Approximation Made Simple. *Phys. Rev. Lett.* **1996**, 77, 3865–3868.
- [31] Perdew, J. P.; Burke, K.; Ernzerhof, M. Reply to Comment on generalized gradient approximation made simple. *Phys. Rev. Lett.* **1998**, *80*, 891.
- [32] Zhang, Y.; Yang, W. Comment on generalized gradient approximation made simple. *Phys. Rev. Lett.* **1998**, *80*, 890.
- [33] Lin, I.-C.; Seitsonen, A. P.; Tavernelli, I.; Rothlisberger, U. Structure and Dynamics of Liquid Water from ab Initio Molecular Dynamics—Comparison of BLYP, PBE, and revPBE

- Density Functionals with and without van der Waals Corrections. *J. Chem. Theory Comput.* **2012**, *8*, 3902–3910.
- [34] Philips, A.; Autschbach, J. Proton NMR Relaxation from Molecular Dynamics: Intramolecular and Intermolecular Contributions in Water and Acetonitrile. *Phys. Chem. Chem. Phys.* **2019**, *21*, 26621–26629.
- [35] Grimme, S. Accurate description of van der Waals complexes by density functional theory including empirical corrections. *J. Comput. Chem.* **2004**, *25*, 1463–1473.
- [36] Grimme, S.; Antony, J.; Ehrlich, S.; Krieg, H. A consistent and accurate ab initio parametrization of density functional dispersion correction (DFT-D) for the 94 elements H-Pu. *J. Chem. Phys.* **2010**, *132*, 154104.
- [37] Marchenko, A.; Duignan, T.; Philips, A.; Badger, T. G.; Ludowieg, H. D.; Moore, B. "Exatomic: A unified platform for computational chemists", https://github.com/exa-analytics/exatomic, doi:10.5281/zenodo.1256873.
- [38] Baerends, E. J.; Ziegler, T.; Autschbach, J.; Bashford, D.; Bérces, A.; Bickelhaupt, F. M.; Bo, C.; Boerrigter, P. M.; Cavallo, L.; Chong, D. P. *et al.* "Amsterdam Density Functional, SCM, Theoretical Chemistry, Vrije Universiteit, Amsterdam, The Netherlands.", URL https://www.scm.com. Accessed 03/17.
- [39] Adamo, C.; Barone, V. Toward reliable density functional methods without adjustable parameters: The PBE0 model. *J. Chem. Phys.* **1999**, *110*, 6158–6170.
- [40] Klamt, A.; Schüürmann, G. COSMO: A new approach to dielectric screening in solvents with explicit expressions for the screening energy and its gradient. *J. Chem. Soc. Perkin Trans.* 2 **1993**, 799–805.
- [41] van Lenthe, E.; Baerends, E. J.; Snijders, J. G. Relativistic regular two-component Hamiltonians. *J. Chem. Phys.* **1993**, *99*, 4597–4610.
- [42] van Lenthe, E.; Baerends, E. J. Density functional calculations of nuclear quadrupole coupling constants in the zero-order regular approximation for relativistic effects. *J. Chem. Phys.* **2000**, *112*, 8279–8292.
- [43] Autschbach, J.; Zheng, S.; Schurko, R. W. Analysis of Electric Field Gradient Tensors at Quadrupolar Nuclei in Common Structural Motifs. *Concepts Magn. Reson. A* **2010**, *36A*, 84–126.

- [44] Glendening, E. D.; Landis, C. R.; Weinhold, F. NBO 6.0: Natural bond orbital analysis program. *J. Comput. Chem.* **2013**, *34*, 1429–1437.
- [45] Glendening, E. D.; Landis, C. R.; Weinhold, F. Natural bond orbital methods. *Wiley Inter-discip. Rev.: Comput.Mol. Sci.* **2012**, *2*, 1–42.
- [46] Pyykkö, P. Year-2017 nuclear quadrupole moments. *Mol. Phys.* **2018**, *116*, 1328–1338.
- [47] Weingärtner, H.; Hertz, H. Magnetic Relaxation by Quadrupolar Interaction of Ionic Nuclei in Non-Aqueous Electrolyte Solutions. Part I. Limiting Values for Infinite Dilution. *Ber. Bunsen-Ges. Phys. Chem.* **1977**, 1204–1221.
- [48] Stengle, T. R.; Reo, N. V.; Williamson, K. L. Nuclear Magnetic Relaxation of Xenon–131 in Solution. The Influence of Solvent Electric Moment and Dynamics on Solute Relaxation. *J. Phys. Chem.* **1984**, *88*, 322–3228.
- [49] Hertz, H. G. Elementary processes in the hydrated shells of ions from proton-relaxation and deuteron relaxation times. *Ber. Bunsen-Ges. Phys. Chem.* **1963**, *67*, 774–786.
- [50] Deverell, C.; Frost, D. J.; Richards, R. E. Quadrupole Relaxation In Solutions Of Electrolytes. *Mol. Phys.* **1965**, *9*, 565–577.
- [51] Endom, L.; Hertz, H. G.; Thul, B.; Zeidler, M. D. A Microdynamic Model Of Electrolyte Solutions As Derived From Nuclear Magnetic Relaxation And Self-Diffusion Data. *Ber. Bunsenges.* **1967**, *71*, 1008–1031.
- [52] Hertz, H. G. Magnetic-Relaxation By Quadrupole Interaction Of Ionic Nuclei In Electrolyte Solutions. 1. Limiting Values For Infinite Dilution. *Ber. Bunsen-Ges. Phys. Chem.* **1973**, 77, 531–540.
- [53] Hertz, H. G. Magnetic-Relaxation By Quadrupole Interaction Of Ionic Nuclei In Electrolyte Solutions. 2. Relaxation At Finite Ion Concentrations. *Ber. Bunsenges.* **1973**, 77, 688–697.
- [54] Schwerdtfeger, P.; Pernpointner, M.; Nazarewicz, W. Calculation of Nuclear Quadrupole Coupling Constants. In *Calculation of NMR and EPR Parameters. Theory and Applications*; Kaupp, M.; Bühl, M.; Malkin, V. G., Eds.; Wiley-VCH: Weinheim, 2004 279–291.
- [55] O'Dell, L.; Schurko, R.; Harris, K.; Autschbach, J.; Ratcliffe, C. Interaction Tensors and Local Dynamics in Common Structural Motifs of Nitrogen: A Solid-state ¹⁴N NMR and DFT Study. *J. Am. Chem. Soc.* **2011**, *133*, 527–546.

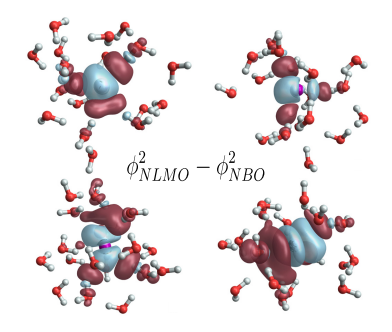
- [56] Brzyska, A.; Woliński, K.; Jaszuński, M. Theoretical studies of the dependence of nuclear quadrupole coupling constants on intermolecular forces. *Comput. Theor. Chem.* **2012**, 983, 54–60.
- [57] Baiocchi, F. A.; Dixon, T. A.; Joyner, C. H.; Klemperer, W. Microwave and radio frequency spectra of Xe-HF. *J. Chem. Phys.* **1981**, *75*, 2041–2046.
- [58] Shen, C.; Anger, E.; Srebro, M.; Vanthuyne, N.; Toupet, L.; Roussel, C.; Autschbach, J.; Reau, R.; Crassous, J. Diastereo- and enantioselective synthesis of organometallic bis(helicene)s by a combination of CH activation and dynamic isomerization. *Chem. Eur. J.* **2013**, *19*, 16722–16728.
- [59] Mallik, B. S.; Semparithi, A.; Chandra, A. A first principles theoretical study of vibrational spectral diffusion and hydrogen bond dynamics in aqueous ionic solutions: D₂O in hydration shells of Cl⁻ ions. *J. Chem. Phys.* **2008**, *129*, 194512.
- [60] Choudhuri, J.; Yadav, V.; Karmakar, A.; Mallik, B.; Chandra, A. A first-principles theoretical study of hydrogen-bond dynamics and vibrational spectral diffusion in aqueous ionic solution: Water in the hydration shell of a fluoride ion. *Pure Appl. Chem.* **2012**, *85*, 27–40.
- [61] Karmakar, A.; Choudhuri, J. R.; Yadav, V. K.; Mallik, B. S.; Chandra, A. A first principles simulation study of vibrational spectral diffusion in aqueous NaBr solutions: Dynamics of water in ion hydration shells. *Chem. Phys.* **2013**, *412*, 13 21.
- [62] Karmakar, A.; Chandra, A. Water in Hydration Shell of an Iodide Ion: Structure and Dynamics of Solute-Water Hydrogen Bonds and Vibrational Spectral Diffusion from First-Principles Simulations. *J. Phys. Chem. B* **2015**, *119*, 8561–8572.
- [63] Lawrence, C. P.; Skinner, J. L. Vibrational spectroscopy of HOD in liquid D₂O. I. Vibrational energy relaxation. *J. Chem. Phys.* **2002**, *117*, 5827–5838.
- [64] Lawrence, C. P.; Skinner, J. L. Vibrational spectroscopy of HOD in liquid D₂O. II. Infrared line shapes and vibrational Stokes shift. *J. Chem. Phys.* **2002**, *117*, 8847–8854.
- [65] Lawrence, C. P.; Skinner, J. L. Vibrational spectroscopy of HOD in liquid D₂O. III. Spectral diffusion, and hydrogen-bonding and rotational dynamics. *J. Chem. Phys.* **2003**, *118*, 264–272.

Table of Contents Synopsis

Adam Philips^a, and Jochen Autschbach*^a

Department of Chemistry
 University at Buffalo

 State University of New York
 Buffalo, NY 14260-3000, USA
 email: jochena@buffalo.edu



Density difference isosurfaces of NLMO minus NBO densities for 5s and 5p iodide orbitals. The iodide-centered NLMOs are distorted and delocalized onto surrounding solvent. Polarization of the iodide density and charge density on surrounding waters contribute to an EFG which drives iodide NMR relaxation.